On the Voltage Ripple Reduction Control of the Linear Switched Reluctance Generator for Wave Energy Utilization

J. F. Pan, Yu Zou, Norbert Cheung, *Senior Member, IEEE*, and Guang-zhong Cao

Abstract—This paper discusses about the voltage output ripple reduction and error minimization for the direct-drive, linear switched reluctance generator (LSRG)-based wave power generation system. First, the concept of the LSRG-based wave power generation system is studied. According to the characteristics of the LSRG, the suitable drive circuit dedicated to proper current excitation and generation is established. Second, the reasons that cause voltage output ripples are investigated. To reduce the remarkable ripples from phase current commutations, a current distribution function (CDF) is proposed based on the minimized copper loss principle. Third, the dual-loop control strategy with current and voltage as the inner and outer loop is constructed, implemented with the proposed CDF. Theoretical bases of the control strategy are derived. The simulation results prove that the proposed control algorithm is capable of voltage ripple suppression and error reduction within the range of ± 0.5 V over the entire operation speed for wave energy extraction, validated by experimental verification.

Index Terms—Current distribution, dual-loop control, linear generator, wave power generation.

I. INTRODUCTION

THE enormous energy potential of ocean waves has been recognized throughout history. As an extractable renewable power source, ocean waves possess approximately more than 1 TW of power [1]. The motions of ocean waves can be ideally recognized as quasi-sinusoidal waveforms and the speed range often falls into 0–2 m/s [2]. Although the early applications of wave power generation have been restricted to coastal regions, from 1994 the offshore methods of both underwater and on the surface of ocean are discovered. However, most of the energy capture manners are based on mechanical linear-to-rotary translators such as the hydraulic or pneumatic converters to transform translational low-speed motion form to high speed. Rotary generators are involved to convert the high-speed form of energy to electricity [3]–[7]. Ocean power technology company owns the commercial product based on a point-capture wave power generation system with pneumatic converters on the surface of water [3]. Offshore, surface wave power generation systems include the Pelamis and the wave dragon [4], [5]. The Archimedes wave swing from BV-AWS [6] is submerged under the water for power generation. The traditional wave power generation methods discussed previously have the disadvantages of complex and expensive system structures. They are hard to maintain and possess low transformation efficiency [7], [8]. Hence, it is difficult to realize a wide market application since the generated electricity from such systems is not cost-effective.

At present, research studies on direct-drive methods have been carried out. By direct capture of wave energy in 1-D, the linear generators are employed to directly transform the low-speed mechanical energy into electricity, thus eliminating intermediate mechanical translators or converters. The direct-drive linear motion systems are proved to be more efficient [8]–[10] compared to the traditional ones discussed previously. According to current research, linear synchronous permanent magnet generators (LSPMGs) are usually employed in the direct-drive power generation system as wave energy converters (WECs). Although the LSPMGs have relatively large force-to-volume ratio and own high efficiency, the involvement of permanent magnets (PMs) results in complicated winding scheme or sophisticated arrangement and assembly of PMs [11]. Therefore, the overall manufacture and assembly cost of such power generation systems is high. In addition, WECs often work under the unattended and rough environment and receive constant bombardment from waves. Temperature variations of the wave energy extraction condition unavoidably affect the operation of the LSPMGs [12]. Furthermore, demagnetization of PMs eventually causes performance degradation or even malfunction of power generation systems [13].

The linear switched reluctance generator (LSRG) is one of the promising candidate WECs without PMs, especially suitable for low-speed operations. It is characterized by a simple machine structure and high robustness, etc. [14]. Furthermore, the total manufacture and assembly cost is low since this type of machines are more suitable for mass production [15]. This feature makes it possible for vast deployment of such WECs to

J. F. Pan and G.-z. Cao are with the Shenzhen Key Laboratory of Electromagnetic Control, Shenzhen University, Shenzhen (e-mail: pan_jian_fei@163.com; cao_guangzhong@163.com).

Y. Zou is with the Shenzhen Key Laboratory of Electromagnetic Control, Shenzhen University, Shenzhen. He is also with the Department of Electrical Engineering, The Hong Kong Polytechnic University, Hong Kong (e-mail: 382724066@qq.com).

N. Cheung is with the Department of Electrical Engineering, The Hong Kong Polytechnic University, Hong Kong (e-mail: norbert_cheung@163.com).

be arranged into matrix forms to extract wave energy from a certain scope and keep the total electricity generation cost at a reasonable price level [16].

For switched reluctance generators (SRGs), physical and control parameters often play an important role for the optimized output in control of the phase current. The control method of the SRG is first introduced in [17], considering their fundamental features. In [18], an optimal control method based on conduction angle range regulation is discussed. However, the ripples of the output voltage are too large for direct connection to the load or the energy storage systems. A voltage control method for the SRG dedicated to wind power applications is proposed [19]. Again the output voltage ripples are not considered, especially the effect of the ripples to forthcoming inversion and the power grid. Since power generation characteristics of SRGs are affected by many contradicted factors, including nonlinear inductance, speed operation range, and back electromagnetic force (EMF), etc. [20]. The conduction angle regulation based on dwell on and off selections alone inevitably leads to output voltage ripples and steady-state errors [21]. To reduce the voltage ripples, in [22], a band-reject filter and a sampling filter based on simulation analysis is studied. However, synchronous sampling inevitably provides large steady-state voltage errors. In order to reduce the effect of parameter variations, the excited range of SRG is controlled by a fuzzy controller [23] to determine the dwell angles of the SRG. According to the previous study, the voltage feedback control method fails as the winding current regulation becomes the single pulsed mode [21]. A dynamic commutation shift controller is proposed to solve the problem. However, the phase current of the SRG is not properly regulated, which is significant to the control precision of the output voltage [17]. For direct-drive wave power generation, the output voltage should be correctly controlled for the LSRGs for direct connection to the load or the energy storage units [24], since the wide speed range of waves has a remarkable influence on the voltage output performance.

This paper mainly focuses on the voltage ripple and steady-state error reduction for the direct-drive LSRG-based power generation system. First, the concept of the direct-drive wave power generation system based on LSRGs is discussed. According to the difference from rotary SRGs, the suitable drive circuit for phase current excitation and generation is established. Since the phase current behavior influences output voltage performance significantly, a current distribution scheme is devised dedicated to the reduction of voltage ripples and steady-state errors. The voltage controller including the current distribution algorithm and the current control loop is designed. With the implementation of the current distribution scheme, voltage output precision within the range of ± 0.5 V can be guaranteed and ripples can be effectively suppressed for the entire operation of wave energy capture.

The paper is organized as follows. The principle of the LSRG-based generation system, the electromagnetic characteristics and the drive circuit for the LSRG are presented in Section II. Then, the detailed analysis of current waveforms and voltage ripples in the chopping mode is discussed, followed by the current distribution function (CDF). Section III investigates the dual-
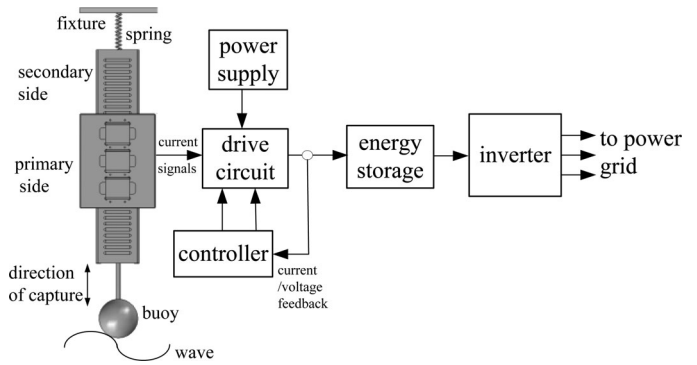

Fig. 1. Schematic of LSRG-based generation system.

loop control system design, implemented with the proposed CDF. Section IV focuses on the simulation of the LSRG system and experimental validation of the control system is provided in Section V. Section VI presents conclusion and discussion.

II. PRINCIPLE OF THE LSRG-BASED GENERATION SYSTEM

A. Concept of the LSRG-Based, Direct-Drive Wave Power Generation System

The overall LSRG-based wave power generation system can be illustrated in Fig. 1. The WEC element can be allocated on the surface or immersed in the water. One end of either the primary side or the secondary side can be connected to the spring and the other end can be linked to the buoy. As the buoy reciprocates with waves, the mechanical energy is absorbed through the LSRG. Phase current signals are transmitted to the drive circuit and the control logic and algorithms are managed by the controller. Voltage signals are the output from the drive circuit in a closed loop manner to interface the energy storage and the inverter, which supplies three-phase alternating current (AC) to the grid.

B. LSRG Structure and Electromagnetic Characteristics

The machine structure and major specifications can be found in Fig. 2 and Table I, respectively. It mainly consists of a stator (secondary side) and three mover units that correspond to a typical "6/4" rotary switched reluctance machine. The movers with windings are fixed on the translator (primary side), supported by two pairs of sliders and one pair of linear guides. Each phase has the same dimensions and ratings, and the phases are defined as A, B, and C, respectively.

The three-dimensional (3-D) flux distribution contour is illustrated in Fig. 3(a). By 3-D FEM calculation, the mutual inductance between any adjacent phases can be plotted in Fig. 3(b). The self-inductance values of any one phase are also calculated with profiles as shown in Fig. 3(c). It is clear that the three phases are considered to be flux decoupled and thus can be controlled independently [8]. The propulsion force waveforms of one phase under different current excitation levels can be found in Fig. 3(d).
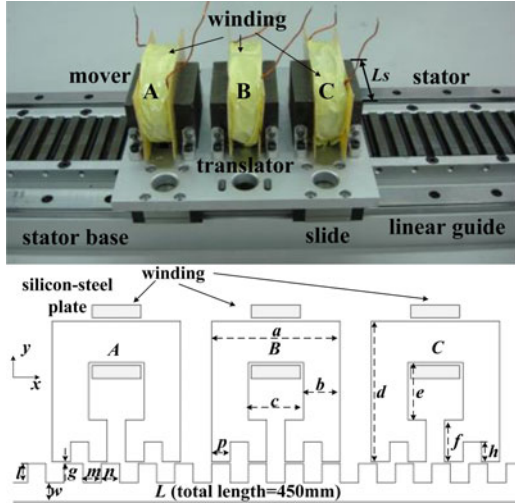
Fig. 2.   LSRG and parameters.

TABLE I
MAJOR MACHINE SPECIFICATIONS

Parameter	Value
Rated power（P）	150 W
Mover teeth width（a）	42 mm
Mover yoke width（b）	12 mm
Mover height（d）	44 mm
Height of winding slot（e）	18 mm
Width of winding slot（c）	18 mm
Mover teeth height（h）	6 mm
Stator teeth width（n）	6 mm
Stator teeth height（l）	6 mm
Stator yoke height（w）	6 mm
Thickness of laminations（s）	0.5 mm
Stack length（Ls）	50 mm
Total length（L）	450 mm
Air gap length（g）	0.3 mm

C. Theoretical Background of the LSRG

The LSRG can be represented as a typical electromechanical system with one mechanical input and three electrical outputs. From the mechanical side [25]

$$F = M\frac{d^2 x}{dt^2} + D\frac{dx}{dt} + f \tag{1}$$

where F stands for the mechanical force input, M is the mass of the translator, x is displacement, D is friction coefficient, and f represents load force. From the electrical terminal, the LSRG can be described in the form of voltage balance equations as [26]

$$u_j = R \cdot i_j + \frac{d\lambda_j}{dt}$$
$$= R \cdot i_j + \left(L_j + i_j\frac{\partial L_j}{\partial i_j}\right) \cdot \frac{di_j}{dt} + i_j \cdot v \cdot \frac{\partial L_j}{\partial x} \quad (j = A, B, C) \tag{2}$$

where u_j, i_j, λ_j, R, and L_j represent the voltage drop, phase current, flux-linkage, resistance, and inductance of the jth winding, respectively. v denotes the velocity of the translator in the x-direction.
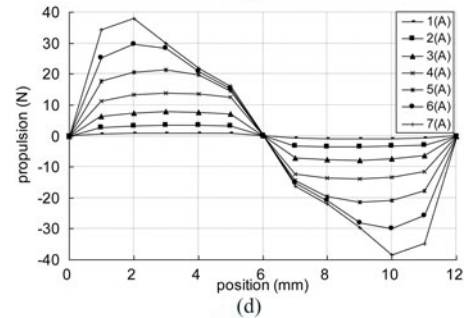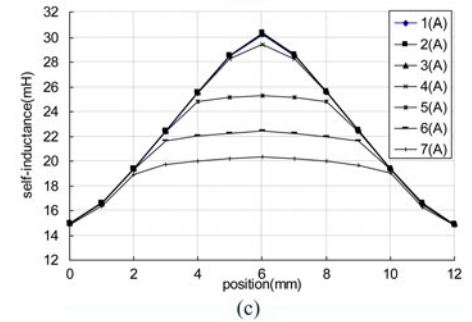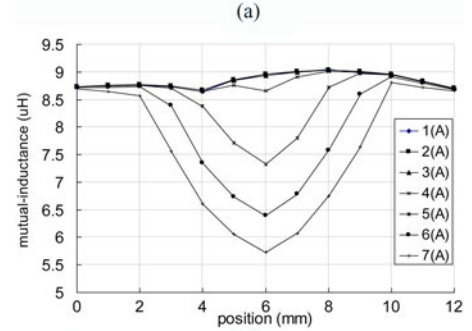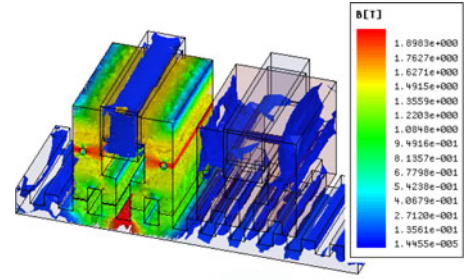

Fig. 3.   (a) 3-D magnetic field distribution (b) mutual inductance, (c) self-inductance and propulsion force output profiles of the LSRG (d).

D. Drive Circuit

Since the operation speed of the LSRG typically falls into 0–2 m/s for wave energy exploitation, the machine works in the low-speed and high-force mode [27]. The back EMF denoted by the third term of (2) is small, and the phase current decreases to zero quickly and flows back to the voltage source during generation period from the typical asymmetric drive topology for rotary SRGs [28]. Therefore, it is unable to sustain the phase currents in such an operation mode. The drive circuit for the LSRG is illustrated in Fig. 4(a). The main difference from the typical drive topology of rotary SRGs lies in the separation of the excitation power supply and the load storage. Each phase of
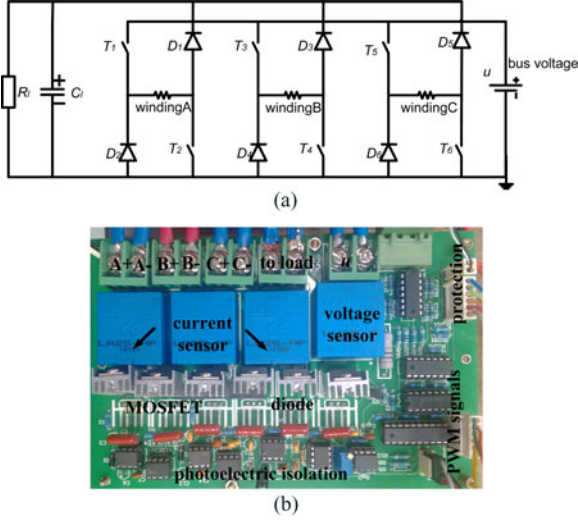
Fig. 4. (a) Drive topology of the LSRG and (b) picture.

the generator is excited by the constant bus voltage *u,* and the generated power is charged into a capacitor and a load resistor in parallel. The initial voltage level across the capacitor is zero. If the power switches T_1 and T_2 of Phase A are turned ON simultaneously, for example, the phase current increases, controlled by the current controller. If T_1 and T_2 are turned OFF, the generated current charges capacitor C_l. The terminal voltage of the capacitor that is equal to load voltage u_l increases quickly from zero. Meanwhile, the current of the load resistance also increases with the terminal voltage. When the second period of excitation of phase A advents, T_1 and T_2 are switched ON again, the capacitor starts to supply power energy for the load and discharge.

The picture of the drive circuit can be found in Fig. 4(b). Pulse-width modulation (PWM) signals are transmitted through the octal bus transceiver 74HC245 to the integrated circuit IR2102. IR2102 and the bus transceiver are isolated by optocouplers CD4504. The power transistors are metal–oxide–semiconductor field-effect transistor (MOSFET) IRF640. The load capacitor is charged by the fast switching diodes MUR1560. Load voltage and phase currents are measured by *LEM* LA25-NP (0.05% of full scale 100 A) and LV25-P (resolution of 0.08% of full scale 500 V), respectively. Protection for overvoltage and overcurrent is also implemented on the drive circuit.

The voltage equation for any one phase thus can be expressed as

$$\begin{cases} u - 2u_T = -e + Ri_j \cdots\cdots\cdots (T_1, T_2 - \text{ON}) \\ u_c + 2u_D = e - Ri_j \cdots\cdots (D_1, D_2 - \text{ON}) \end{cases} \quad (3)$$

where u_c, u_T, and u_D are the voltage drop across the capacitor, transistors, and diodes, respectively. e is the back EMF.

E. Phase Current Waveforms in the Chopping Mode and Voltage Ripples

Due to the nonlinear winding inductance, phase current waveforms are hard to maintain ideal square shapes and they fluctuate

severely upon commutation between phases. According to (3), the phase current waveforms from PWM regulation can be obtained in two steps. The first step is phase magnetization as T_1 and T_2 are switched ON. The second step is diode freewheeling process through D_1 and D_2 once T_1 and T_2 are OFF. Phase current can be derived as

$$\begin{cases} i_j = i_{\text{init}} + \dfrac{u \cdot \Delta x}{v \cdot L_j}(T_1, T_2 - \text{ON}) \\ i_j = i_{\text{init}} e^{-\frac{R_l C_l \cdot \Delta x}{v}}(D_1, D_2 - \text{ON}) \end{cases} \quad (4)$$

where i_{init} is the initial current value, Δx is the displacement of the translator, and R_l is the load resistance. Take phase A for example, the voltage balance equation can be rewritten as (5) considering the mutual inductance of adjacent two phases, according to (2)

$$u_A = R \cdot i_A + \frac{d\lambda_A}{dt} = R \cdot i_A + \left(L_A + i_A \frac{\partial L_A}{\partial i_A}\right) \cdot \frac{di_A}{dt} + i_A$$

$$\cdot v \cdot \frac{\partial L_A}{\partial x} + \left(M + i_B \frac{\partial M}{\partial i_B}\right) \cdot \frac{di_B}{dt} + i_B \cdot v \cdot \frac{\partial M}{\partial x} \quad (5)$$

where M denotes the mutual inductance of phase A and B. i_A and i_B are currents of phases A and B, respectively. Substitute (5) into (3), the change of phase current A with respect to the position of translator can be further derived as the following equation, by neglecting the influence of current on self-inductance:

$$\begin{cases} \dfrac{di_A}{dt} = \left(u_A - 2u_T - R \cdot i_A - i_A \cdot v \cdot \dfrac{\partial L_A}{\partial x} - M \cdot \dfrac{di_B}{dt}\right. \\ \qquad \left. + i_B \cdot v \cdot \dfrac{\partial M}{\partial x}\right) \Big/ L_A (T_1, T_2 - \text{ON}) \\ \dfrac{di_A}{dt} = \left(u_c + 2u_D + R \cdot i_A - i_A \cdot v \cdot \dfrac{\partial L_A}{\partial x} - M \cdot \dfrac{di_B}{dt}\right. \\ \qquad \left. + i_B \cdot v \cdot \dfrac{\partial M}{\partial x}\right) \Big/ L_A (D_1, D_2 - \text{ON}). \end{cases} \quad (6)$$

It is obvious that increasing self-inductance values can reduce the change of phase current, and the mutual inductance has a negative impact on decreasing the change rate of phase current. The bigger the value of mutual inductance, the greater the influence of phase B has on the change rate of current from phase A. Therefore, the mutual inductance is one of the main factors on ripple generation of the phase current.

According to the load circuit of the system, the output voltage is

$$u_l(t) = \frac{1}{C} \int i_{c_l}(t) dt = R_l \cdot i_R(t) \quad (7)$$

where $i_l(t) = i_{c_l}(t) + i_{R_l}(t)$. It can be concluded that the current output contributes to the ripples of the output voltage as well. Since the LSRG operates in the low-speed range for entire wave energy capture, the PWM control method can be adopted for the whole region as the change rate of self-inductance is negative. The operation range is composed of the excitation and power generation region. When T_1 and T_2 are switched ON simultaneously, the windings of LSRG are excited (excitation region). After T_1 and T_2 are OFF and D_1 and D_2 are turned ON, the LSRG enters the generation region. The typical voltage
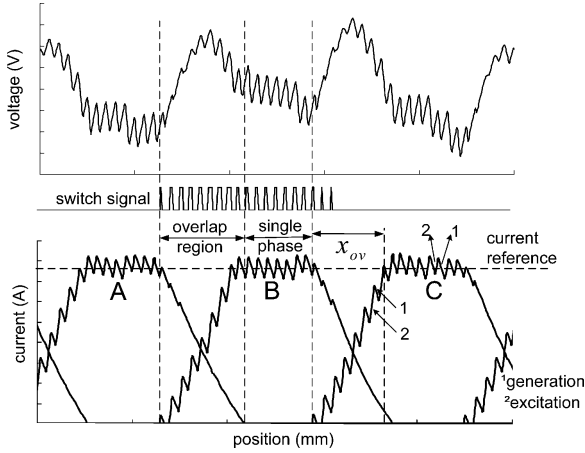
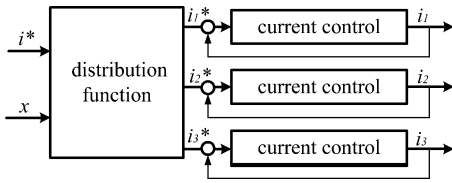Fig. 5.   Typical current waveforms and voltage ripples of the LSRG.

Fig. 6.   Current distribution with closed loop control.

and current waveforms can be obtained from FEM as shown in Fig. 5.

The voltage ripples are mainly caused by two reasons: one is by the current transition waveforms during single-phase operation; the other originates from the commutations between phases (the overlap region). The ripples from the first one can be alleviated by adding a capacitor in parallel with the freewheeling diodes if the frequency of PWM is high enough [19]. The ripples can be further reduced if the phase current can be properly regulated [29]. The ripples caused by the second reason can be alleviated by correct allocation of phase currents during commutations, applying proper closed-loop current control regulation strategies.

F. Current Distribution Method

It is clear that voltage ripples caused by phase current commutations as shown in Fig. 5 are comparatively larger than those from single phase transitions. In combination of the current distribution scheme, closed loop control strategies can be cascaded to the CDF block to reduce the ripples caused by both single phase transitions and phase commutations, as shown in Fig. 6.

If the conversion efficiency of the LSRG is denoted as η, the energy conversion equation for any phase of the LSRG can be expressed as

$$F \cdot v \cdot \eta = P = u_l \cdot i_l \tag{8}$$

where P is the output power, u_l and i_l are the total output voltage and current (current sum of resistor and capacitor) from load, respectively. In the linear region, the previous equation can be

rewritten as [30]

$$\frac{1}{2} \cdot i \cdot \frac{dL}{dx} \cdot v \cdot \eta = u_l. \tag{9}$$

It can be concluded that if the value of $i \cdot \frac{dL}{dx}$ is constant, the output voltage remains unchanged as the product of velocity and efficiency is invariant. If two phases commutate simultaneously during the overlap region, the above equation can be rewritten as

$$i \cdot \frac{dL}{dx} = i_j \cdot \frac{dL_j}{dx} + i_{j+1} \cdot \frac{dL_{j+1}}{dx} = k \cdot u_l \tag{10}$$

where $k = \frac{2}{v \cdot \eta}$. As two phases are commutated, the copper loss of the LSRG can be expressed as

$$P_{\text{copperloss}} = \int_{x_{\text{on}}}^{x_{\text{on}}+x_{\text{ov}}} i_j^2 dx + \int_{x_{\text{on}}}^{x_{\text{on}}+x_{\text{ov}}} i_{j+1}^2 dx \tag{11}$$

where x_{on} and x_{ov} are the length of the single phase and overlap region, as denoted in Fig. 5 In order to ensure the minimized copper loss of the LSRG, the function of $m = i_j^2 + i_{j+1}^2$ should be kept as minimum [31], [32]. Let $f_1 = \frac{dL_j}{dx}$ and $f_2 = \frac{dL_{j+1}}{dx}$, then the phase current follows the equations as

$$i_j \cdot f_1 + i_{j+1} \cdot f_2 = k \cdot u_l. \tag{12}$$

The Lagrange function of $m = i_j^2 + i_{j+1}^2 + \alpha(i_j \cdot f_1 + i_{j+1} \cdot f_2 - k \cdot u_l)$ can be constructed and the partial derivative of m can be expressed as

$$\begin{cases} \dfrac{\partial m}{\partial i_j} = 2i_j + \alpha f_1 = 0 \\[2mm] \dfrac{\partial m}{\partial i_{j+1}} = 2i_{j+1} + \alpha f_2 = 0 \\[2mm] \dfrac{\partial m}{\partial \alpha} = i_j \cdot f_1 + i_{j+1} \cdot f_2 - k \cdot u_l = 0. \end{cases} \tag{13}$$

Therefore, current of each phase in the overlap region can be derived as

$$\begin{cases} i_j = \dfrac{k \cdot u_l \cdot f_1}{f_1^2 + f_2^2} \\[3mm] i_{j+1} = \dfrac{k \cdot u_l \cdot f_2}{f_1^2 + f_2^2}. \end{cases} \tag{14}$$

The commutation region and value for each phase can be summarized as listed in Table II with zero displacement defined as the fully aligned position of phase A.

The self-inductance value of the LSRG can be expressed as [33]

$$\begin{cases} L_A = L_a + L_\Delta \cos(2\pi \cdot x/\tau) \\ L_B = L_a + L_\Delta \cos(2\pi \cdot x/\tau - 2\pi/3) \\ L_C = L_a + L_\Delta \cos(2\pi \cdot x/\tau - 4\pi/3) \end{cases} \tag{15}$$

where $L_a = 22$ mH is the average self-inductance value, and $L_\Delta = 7.5$ mH is the half-value of the difference between maximum and minimum self-inductance. τ denotes the pole-pitch of the LSRG (12 mm). The change rate of the self-inductance can

TABLE II
COMMUTATION REGION AND VALUE FOR EACH PHASE

position	velocity >0		velocity <0	
	phase	value	phase	value
0mm-2mm	A,C	f_{AC}, f_{CA}	B	u_l / f_B
2mm-4mm	A	u_l / f_A	B,C	f_{BC}, f_{CB}
4mm-6mm	A,B	f_{AB}, f_{BA}	C	u_l / f_C
6mm-8mm	B	u_l / f_B	C,A	f_{CA}, f_{AC}
8mm-10mm	B,C	f_{BC}, f_{CB}	A	u_l / f_A
10mm-12mm	C	u_l / f_C	A,B	f_{AB}, f_{BA}

Note: $f_{ij} = \dfrac{u_l \cdot f_i}{f_i^2 + f_j^2}$ $i, j = A, B, C.$

thus be obtained as

$$\begin{cases} f_A = -2\pi L_\Delta \sin(2\pi \cdot x/\tau)/\tau \\ f_B = -2\pi L_\Delta \sin(2\pi \cdot x/\tau - 2\pi/3)/\tau \\ f_C = -2\pi L_\Delta \sin(2\pi \cdot x/\tau - 4\pi/3)/\tau. \end{cases} \quad (16)$$

According to Table II the current distribution parameters for phase A can be further expressed as

$$C_{f_A} =$$

$$\begin{cases} -\dfrac{\sin(2\pi \cdot x/\tau)}{2\pi L_\Delta \cdot (\sin^2(2\pi \cdot x/\tau) + \sin^2(2\pi \cdot x/\tau - 4\pi/3))/\tau} & 0 \le x < 2 \\[4mm] -\dfrac{1}{2\pi L_\Delta \cdot \sin(2\pi \cdot x/\tau)/\tau} & 2 \le x < 4 \\[4mm] -\dfrac{\sin(2\pi \cdot x/\tau)}{2\pi L_\Delta \cdot (\sin^2(2\pi \cdot x/\tau) + \sin^2(2\pi \cdot x/\tau - 2\pi/3))/\tau} & 4 \le x < 6. \end{cases} \quad (17)$$

It is clear that CDF depends mainly on the change rate of the self-inductance of the phases.

Based on the previous analysis, the interval x_{ov} from the overlap region of two commutation phases must satisfy the following equation:

$$x_{ov} = \frac{v \cdot \lambda_s}{u} \quad (18)$$

where λ_s is the desired flux linkage. During magnetization, the phase current must rise to the desired flux-linkage value to build up the magnetic field; the phase current also needs to decline to zero in the demagnetization period, as indicated by Fig. 5. x_{ov} represents the requirement for magnetization and demagnetization period under different operation speeds.

III. CONTROL SYSTEM DESIGN

The whole power generation system can be illustrated in Fig. 7 It is mainly composed of the mechanical input, the drive circuit with load, and the control part. Mechanical input is provided from a controllable linear PM motor with its prime mover connected to the translator of the LSRG. Phase current i_j from
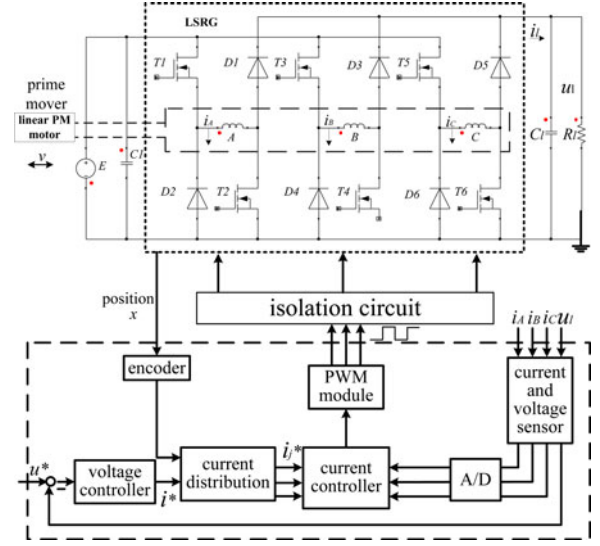

Fig. 7. Power generation control system.

A to C and total current i_l from the three phases and load are collected by current sensors and fed back to the current controller. The voltage controller receives the actual voltage and compares with the reference signal u^*. Current reference i^* from the voltage controller and position x are input to the CDF block for calculation of current commands for the three phases. Meanwhile, the current commands are compared with the actual current values to determine the duty cycles of the PWM signals, which are transmitted through the isolation circuit to control the state of the power transistors $T_1 - T_6$.

The ultimate goal for the control system is to reduce voltage ripples and obtain small steady-state errors under different speed operations. The voltage regulation scheme is based on the dual-loop control methodology with current and voltage control as the inner and outer loop, respectively. Both control loops employ the proportional integral (PI) algorithm for current and voltage regulation. The control diagram can be represented as shown in Fig. 8(a). G_{c_u} and G_{c_i} stand for the transfer function of the voltage and current controller, respectively. The voltage controller outputs current command and the output from the current controller is the calculated duty cycles for the three phases. The total generated current will be injected to the load. F_i and F_u represent the transfer function of the current and voltage feedback.

A. Current Control

The current control loop is applied to regulate the phase current, modulated by the PWM method. The current control block diagram of any one phase is shown in Fig. 8(b). Duty cycle K_D is the proportion of the bus voltage to the maximum voltage output, denoted as

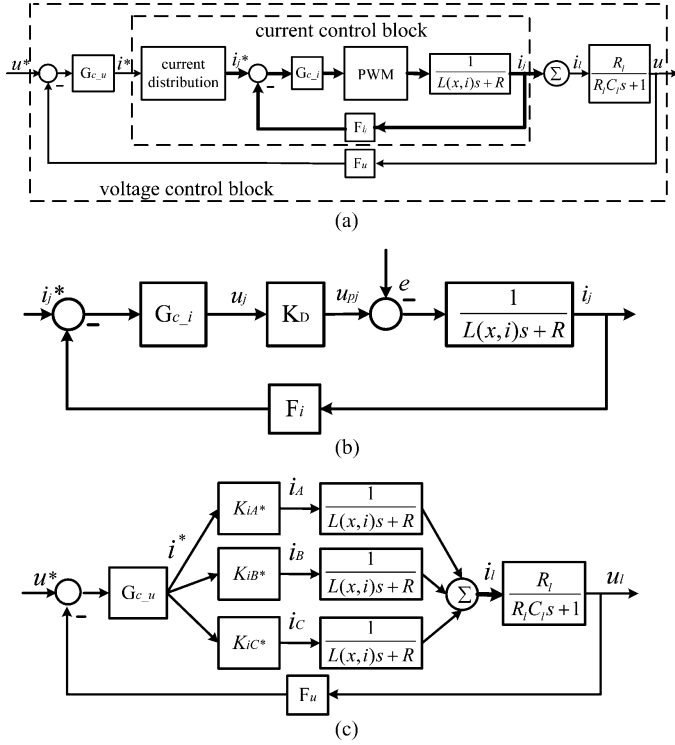$$K_D = \frac{u}{u_{\max}} \quad (19)$$

(a)

(b)

(c)

Fig. 8.   (a) Dual loop control diagram, (b) current, and (c) voltage control block.

where u_{pj} is the terminal phase voltage. The transfer function of the PI controller is formulated as [34]

$$G_{c\_i} = \frac{K_p(s + K_i)}{s}. \tag{20}$$

The closed-loop transfer function can thus be represented as

$$G_i = \frac{i_j}{i_j^*} = \frac{\frac{K_D K_p}{L}(s + K_i)}{s^2 + \frac{(R + F_i K_D K_p)s}{L} + \frac{F_i K_D K_p K_i}{L}} \tag{21}$$

Since $F_i K_D K_p \gg R$, (16) can be further rewritten as

$$G_i = \frac{i}{i^*} = \frac{K_D K_p(s + K_i)/L}{s^2 + (F_i K_D K_p/L)s + F_i K_D K_p K_i/L}. \tag{22}$$

According to a typical second-order system, let $F_i = 1$, then we have

$$K_i = \frac{\omega_n}{2\xi}, \quad K_p = \frac{2 \cdot \xi \cdot \omega_n L}{K_D}$$

where

$$\omega_n = \sqrt{\frac{F_i K_D K_p K_i}{L}}, \quad \xi = \frac{1}{2} \cdot \sqrt{\frac{F_i K_D K_p}{K_i L}}.$$

B. Voltage Control

Considering that the delay time of the outer voltage loop is much slower than the inner current loop [35], the current loop can be simplified as a proportion unit K_{i^*}, as depicted in Fig. 8(c). If the PI algorithm is employed, then $G_{c\_u} = (K_{pv}s + K_{iv})/s$. The voltage closed loop transfer function can
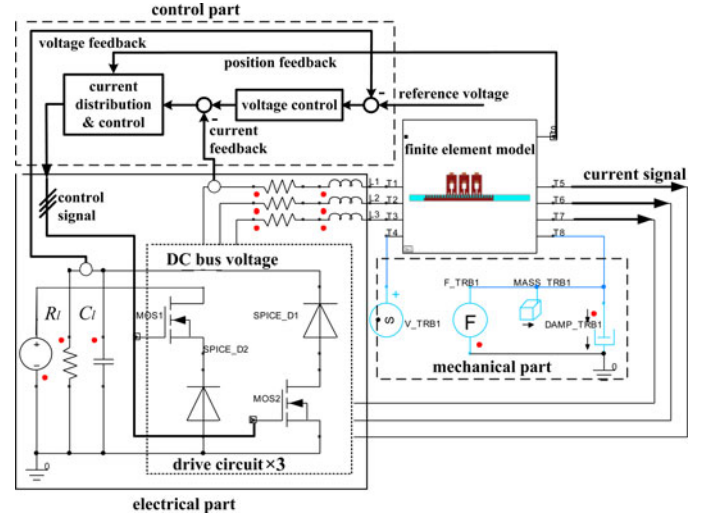

Fig. 9.   Control system structure.

thus be formulated as $(F_u = 1)$,

$$\frac{u_l}{u^*} =$$

$$\frac{\left(R + K_{pv}R_l K_i^*\right)s + K_{iv}K_{i^*}R_l}{LR_l C_l s^3 + (L + RR_l C_l)s^2 + \left(R + K_{pv}K_i^*R_l\right)s + K_{iv}K_{i^*}R_l} \tag{23}$$

with $K_i^* = K_{iA}^* + K_{iB}^* + K_{iC}^*$. Voltage error transfer function can obtained as

$$\frac{\Delta u}{u^*} = \frac{LC_l s^3 + R_l C_l s^2}{LC_l s^3 + R_l C_l s^2 + K_{i^*}K_{pv}s + K_{i^*}K_{iv}}. \tag{24}$$

IV. SIMULATION RESULTS

Simulation analysis is performed based on the multiphysics environment by cosimulation of *Maxwell* and *Simplorer* software package. The control structure is illustrated in Fig. 9. The finite-element model of the LSRG designed in *Maxwell* is connected to the electrical part and the mechanical part, which are constructed in *Simplorer* environment. Control algorithms are programmed in *Simplorer*. The control part includes voltage and current control with the CDF. The Current, voltage, and position feedback are obtained from the calculation results of the electrical part and the finite-element model, respectively. The electrical part mainly consists of a dc power source, the drive circuit, and the load resistance and capacitance. The electrical part is responsible for receiving switch signals from the control part and turns on or off the power transistors for the three phases correctly. Current signals from corresponding phases are transmitted to drive the LSRG FEM model. Mechanical input is configured in *Maxwell* with programmable velocity reference to the LSRG. The mechanical part consists of the mass of the mover and a damper, to simulate the physical characteristics of the LSRG. The sampling rates of the current and voltage loop are set as 2 KHz and 1 KHz, respectively.

The voltage reference level is set as 12 V for standard interface to energy storage systems. The step response with PWM
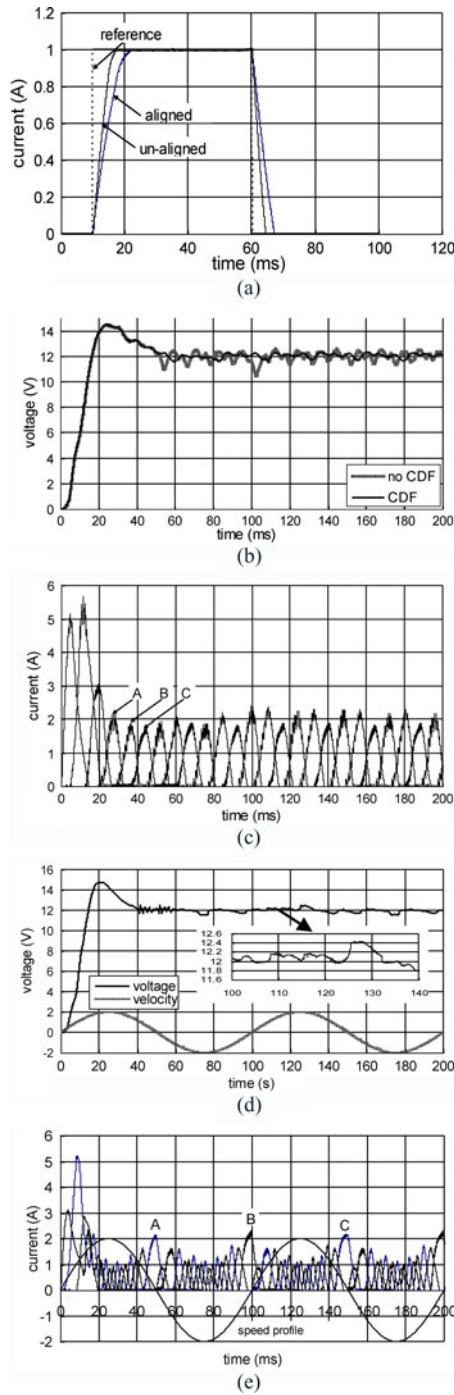
Fig. 10. (a) Current, (b) voltage step response, (c) phase current waveforms under step command, (d) voltage response, and (e) phase current waveforms under the variable speed.

TABLE III
CONTROL PARAMETERS FOR CURRENT AND VOLTAGE CONTROL

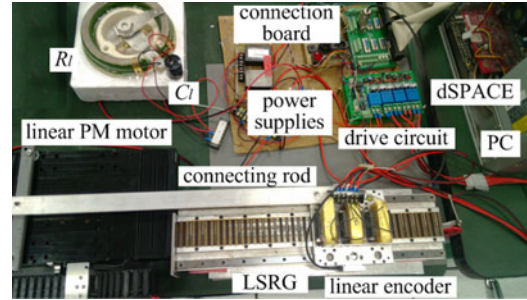| Parameter	P	I
current loop	0.2	0.5
voltage loop	0.9	0.4

Fig. 11. Experimental setup.

The voltage step response can be derived as shown in Fig. 10(b) in the case of CDF and no CDF situation, with control parameters tabulated in Table III The current waveforms for three phases under the voltage step command can be found in Fig. 10(c). The absolute steady-state error of 0.5 V can be achieved. The simulation for the power generation system under various speeds with sinusoidal operation from 0 to 10 Hz with amplitude of 2 m/s is performed as shown in Fig. 10(d). It can be concluded that it takes about 60 ms for the voltage response to settle and the precision of ± 0.5 V can be obtained despite the dynamic velocity. It can be concluded that large dynamic errors appear as the speed is fast. Large speed values lead to longer time regulation for the elimination of errors. From the phase current profiles depicted in Fig. 10(e), current amplitude is relatively small when the speed value is large, due to the significance of the back EMF value.

V. EXPERIMENTAL VERIFICATION

The overall control setup can be found in Fig. 11. The experiment is performed based on the real-time control platform of dSPACE DS1104 board. Control algorithms are developed under MATLAB/Simulink which can be downloaded to the DSP of the control board. The current and voltage feedback signals are collected by analog-to-digital channels on the control board. Position information is provided by the linear optical encoder with the resolution of 1 μm, interfaced through the quadrature encoder pulse channel. Current output is realized by the PWM modules of the control board. Mechanical wave motions are simulated by a commercial linear PM motor, connected to the translator of the LSRG by the rod. Frequency of the PWM, current, and voltage sampling are configured as 10, 2, and 1 kHz, respectively. Control parameters correspond to those from the simulation analysis in Table III The load is composed of a tunable power resistor and capacitor in parallel with values of 10 Ω and 3300 μF, respectively.

The current unit step response profiles for any one phase at fully aligned and unaligned positions can be found in Fig. 12. Due to the response time of the current sensors, the rise time

regulation of current waveforms from any one phase at 0.5 m/s can be found in Fig. 10(a). It is clear that the frequency of 10 kHz PWM is fast enough for current to settle at different mover positions. The control parameters for the current control loop thus can be derived as shown in Table III After a proper transient of 30 ms, the current profiles reach the steady states with small fluctuations.
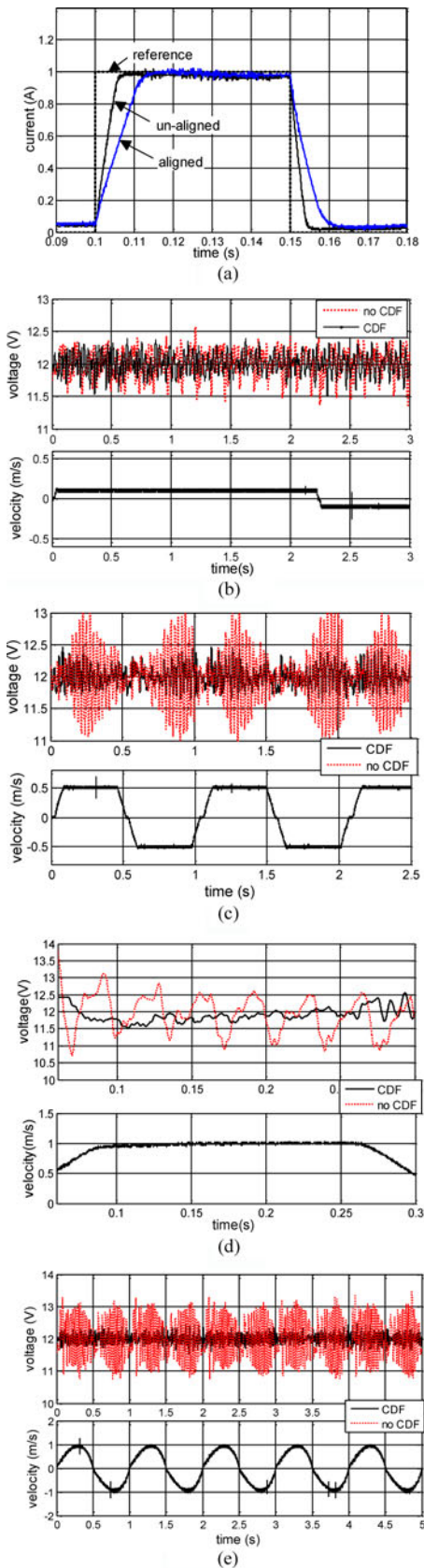
Fig. 12. (a) Current unit step response, voltage response under (b) 0.1/ms, (c) 0.5/ms, and (d) 1/ms, and (e) the variable speed.

is longer compared to the simulation results. There are steady-states errors with the value of 0.05 A, owing to the precision of the current sensor.

The voltage output response under speed operation of 0.1, 0.5, and 1 m/s can be found in Fig. 12(b)–(d). Due to the power and physical limitations of the linear PM machine, it takes some time for the motor to accelerate and decelerate until it reaches the destination speed with certain variations. It can be concluded that the voltage can be controlled with the precision of ± 0.5 V under the dual-loop control scheme with the CDF. However, the steady-state errors are large for the voltage profiles without CDF, especially at high-speed operations. This is mainly caused by large back EMF values and power generation enters the single-phase mode operation at high speed when the phase current becomes difficult to be activated and controlled [21].

VI. CONCLUSION AND DISCUSSION

This paper proposes a current distribution scheme for voltage ripple minimization and error reduction for the LSRG based, direct-drive, wave power generation system over the entire speed operation range. The drive circuit that ensures proper phase current excitation and generation for the LSRG is developed. The dual-loop control strategy with current and voltage as the inner and outer control loop is implemented, employing the proposed CDF. Simulation analysis proves that the voltage ripple can be effectively suppressed and an absolute dynamic error of 0.5 V can be achieved despite variable speed operations. Due to the limitations of the linear PM motor as the mechanical input, the experimental results verify that the control strategy with the CDF is capable of voltage control within the range of ± 0.5 V under the operation of 0 to 1 m/s. The voltage control performance from this paper contributes to the improvement of the signal quality for the inversion unit and the interface to the power grid, for the forthcoming utilization of the generated electricity from the direct-drive wave energy extraction system.

The authors consider that voltage control performance is dependent on the precision of the voltage and current sensors, especially the resolution of the current sensors. The control algorithms for current and voltage regulations influence the voltage output performance as well. More advanced control strategies can be developed for the power generation system in the near future. It can also be expected that the LSRG based power generation systems find their commercial values for wave energy exploitation.

REFERENCES

[1] R. Bhattacharyya and M. E. McCormick, *Wave Energy Conversion, Ocean Engineering Series*, vol. 6.   Oxford, U.K.: Elsevier, 2003, pp. 1–10.

[2] J. Scruggs and P. Jacob, "Harvesting ocean wave energy," *Science*, vol. 323, pp. 1176–1178, 2009.

[3] T. Ahmed, K. Nishida, and M. Nakaoka, "Grid power integration technologies for offshore ocean wave energy," in *Proc. IEEE Energy Convers. Congr. Expo. Conf.*, 2010, pp. 2378–2385.

[4] W. D. Jones, "Update—Ocean power catches a wave," *IEEE Spectrum*, vol. 45, no. 7, pp. 14–27, Jul. 2008.

[5] D. L. O'Sullivan and A. W. Lewis, "Generator selection and comparative performance in offshore oscillating water column ocean wave energy converters," *IEEE Trans. Energy Convers.*, vol. 26, no. 2, pp. 603–614, Jun. 2011.

[6] H. Polinder, M. E. C. Damen, and F. Gardner, "Linear PM generator system for wave energy conversion in the AWS," *IEEE Trans. Energy Convers.*, vol. 19, no. 3, pp. 583–589, Sep. 2004.

[7] A. Nasiri, S. A. Zabalawi, and D. C. Jeutter, "A linear permanent magnet generator for powering implanted electronic devices," *IEEE Trans. Power Electron.*, vol. 26, no. 1, pp. 192–199, Jan. 2011.

[8] S. W. Zhao, N. C. Cheung, W. Gan, and J. Yang, "High-precision position control of a linear-switched reluctance motor using a self-tuning regulator," *IEEE Trans. Power Electron.*, vol. 25, no. 11, pp. 2820–2827, Nov. 2010.

[9] C. Cheun, "TSK-type self-organizing recurrent-neural-fuzzy control of linear microstepping motor drives," *IEEE Trans. Power Electron.*, vol. 25, no. 9, pp. 2253–2265, Sep. 2010.

[10] C. Cheun, "Supervisory interval type-2 TSK neural fuzzy network control for linear microstepping motor drives with uncertainty observer," *IEEE Trans. Power Electron.*, vol. 26, no. 7, pp. 2049–2064, Jul. 2011.

[11] J. Prudell, M. Stoddard, E. Amon, T. K. A. Brekken, and A. Jouanne, "A permanent-magnet tubular linear generator for ocean wave energy conversion," *IEEE Trans. Ind. Appl.*, vol. 46, no. 6, pp. 2392–2400, Nov./Dec. 2010.

[12] C. Kral, A. Haumer, and S. Lee, "A practical thermal model for the estimation of permanent magnet and stator winding temperatures," *IEEE Trans. Power Electron.*, vol. 29, no. 1, pp. 455–464, Jan. 2014.

[13] I. Stamenkovic, N. Milivojevic, N. Schofield, and M. Krishnamurthy, "Design, analysis, and optimization of ironless stator permanent magnet machines," *IEEE Trans. Power Electron.*, vol. 28, no. 5, pp. 2527–2538, May 2013.

[14] S. K. Sahoo, S. Dasgupta, S. K. Panda, and J. Xu, "A lyapunov function-based robust direct torque controller for a switched reluctance motor drive system," *IEEE Trans. Power Electron.*, vol. 27, no. 2, pp. 555–564, Feb. 2012.

[15] J. Kim and R. Krishnan, "Single-controllable-switch-based switched reluctance motor drive for low cost, variable-speed applications," *IEEE Trans. Power Electron.*, vol. 27, no. 1, pp. 379–387, Sep. 2012.

[16] J. Pan, Y. Zou, and G. Cao, "Investigation of a low-power, double-sided switched reluctance generator for wave energy conversion," *IET Renew. Power Generation*, vol. 7, no. 2, pp. 98–109, 2013.

[17] Y. Sozer and D.A. Torrey, "Closed loop control of excitation parameters for high speed switched-reluctance generators," *IEEE Trans. Power Electron.*, vol. 19, no. 2, pp. 355–362, Mar. 2004.

[18] S. Narla, Y. Sozer, and I. Husain, "Switched reluctance generator controls for optimal power generation and battery charging," *IEEE Trans. Ind. Appl.*, vol. 48, no. 5, pp. 1452–1459, Sep. 2012.

[19] R. Cárdenas, R. Peña, M. P. Clare, G. Asher, and P. Wheeler, "Control of a switched reluctance generator for variable-speed wind energy applications," *IEEE Trans. Energy Convers.*, vol. 20, no. 4, pp. 781–791, Dec. 2005.

[20] Y. Chang and C. Liaw, "Establishment of a switched-reluctance generator-based common DC microgrid system," *IEEE Trans. Power Electron.*, vol. 26, no. 9, pp. 2512–2527, Sep. 2011.

[21] Y. Chang and C. Liaw, "On the design of power circuit and control scheme for switched reluctance generator," *IEEE Trans. Power Electron.*, vol. 23, no. 1, pp. 445–454, Jan. 2008.

[22] D. B. Wicklund and D. S. Zinger, "Voltage feedback signal conditioning in switched reluctance generation systems," in *Proc. IEEE Appl. Power Electron. Conf.*, 2000, pp. 376–380.

[23] H. Chen and J. J. Gu, "Implementation of the three-phase switched reluctance machine system for motors and generators," *IEEE/ASME Trans. Mechatronics*, vol. 15, no. 3, pp. 421–432, Jun. 2010.

[24] H. Geng, D. Xu, B. Wu, and W. Huang, "Direct voltage control for a stand-alone wind-driven self-excited induction generator with improved power quality," *IEEE Trans. Power Electron.*, vol. 26, no. 8, pp. 2358–2368, Aug. 2011.

[25] J. Chai and Y. C. Liaw, "On the switched-reluctance motor drive with three-phase single-switch switch-mode rectifier front-end," *IEEE Trans. Power Electron.*, vol. 25, no. 5, pp. 1135–1148, May 2010.

[26] P. Shamsi and B. Fahimi, "Single-bus star-connected switched reluctance drive," *IEEE Trans. Power Electron.*, vol. 28, no. 12, pp. 5578–5597, Dec. 2013.

[27] J. Du, D. Liang, L. Xu, and Q. Li, "Modeling of a linear switched reluctance machine and drive for wave energy conversion using matrix and tensor approach," *IEEE Trans. Magn.*, vol. 46, no. 6, pp. 1334–1337, Jun. 2010.

[28] H. Torkaman and E. Afjei, "Comprehensive detection of eccentricity fault in switched reluctance machines using high-frequency pulse injection," *IEEE Trans. Power Electron.*, vol. 28, no. 3, pp. 1382–1390, Mar. 2013.

[29] X. D. Xue, K. W. E. Cheng, and S. L. Ho, "Optimization and evaluation of torque-sharing functions for torque ripple minimization in switched reluctance motor drives," *IEEE Trans. Power Electron.*, vol. 24, no. 9, pp. 2076–2090, Sep. 2009.

[30] L. O. Henriques, L. G. Rolim, W. Suemitsu, J. A. Dente, and P. J. Branco, "Development and experimental tests of a simple neurofuzzy learning sensorless approach for switched reluctance motors," *IEEE Trans. Power Electron.*, vol. 26, no. 11, pp. 3330–3334, Nov. 2011.

[31] V. P. Vujičić, "Minimization of torque ripple and copper losses in switched reluctance drive," *IEEE Trans. Power Electron.*, vol. 27, no. 1, pp. 388–399, Jan. 2012.

[32] H. J. Brauer, M. D. Hennen, and R. W. De Doncker, "Control for polyphase switched reluctance machines to minimize torque ripple and decrease ohmic machine losses," *IEEE Trans. Power Electron.*, vol. 27, no. 1, pp. 370–378, Jan. 2012.

[33] J. Cai and Z. Deng, "Sensorless control of switched reluctance motor based on phase inductance vectors," *IEEE Trans. Power Electron.*, vol. 27, no. 7, pp. 3410–3423, Jul. 2012.

[34] Z. Chen, "PI and sliding mode control of a cuk converter," *IEEE Trans. Power Electron.*, vol. 27, no. 8, pp. 3695–3703, Aug. 2012.

[35] A. Luo, F. Ma, C. Wu, S. Ding, Q.-C. Zhong, and Z. Shuai, "A dual-loop control strategy of railway static power regulator under V/V electric traction system," *IEEE Trans. Power Electron.*, vol. 26, no. 7, pp. 2079–2091, Jul. 2011.

J. F. Pan received the Ph.D. degree from the Department of Electrical Engineering, Hong Kong Polytechnic University in Hong Kong, in 2006.

He is currently in College of Mechatronics and Control Engineering, Shenzhen University, Shenzhen, China. His main research interests include design and control of switched reluctance motors and generators.
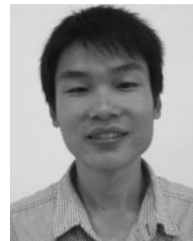
Yu Zou received the B.S. degree from the Hubei University, Wuhan, China, in 2010, and the master's degree from the Shenzhen Universtiy, Shenzhen, China, in 2013.

He is a research personnel with the Department of Electrical Engineering, Hong Kong Polytechnic University and Shenzhen Key Laboratory of Electromagnetic Control, Shenzhen University.

Norbert Cheung (S'95–M'97–SM'05) received the B.Sc. degree from the University of London, London, U.K., the M.Sc. degree from the University of Hong Kong, Hong Kong, and the Ph.D. degree from the University of New South Wales, Sydney, Australia, in 1981, 1987, and 1995, respectively.

He is currently with the Department of Electrical Engineering, Hong Kong Polytechnic University, Kowloon, Hong Kong. His research interests include motion control, actuator design, and power electronic drives.
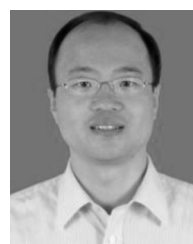
Guang-zhong Cao received the B.S., M.S., and the Ph.D. degrees in electrical engineering and automation from Xi'an Jiaotong University, Shanxi, China.

He is currently a Professor with the Department of Control Engineering, Shenzhen University, Shenzhen, China. He has published more than 60 articles in refereed journals and conferences. His research interests include embedded systems, motor control, data acquisition units, and automatic detection systems.